Optical multi-stability in a nonlinear high-order microring resonator filter

Article (Published Version)

APL Photonics

Optical multi-stability in a nonlinear high-order microring resonator filter

Cite as: APL Photonics 5, 056106 (2020); https://doi.org/10.1063/5.0002941
Submitted: 29 January 2020 . Accepted: 05 May 2020 . Published Online: 22 May 2020

Li Jin, Luigi Di Lauro, Alessia Pasquazi, Marco Peccianti, David J. Moss, Roberto Morandotti, Brent E. Little, and Sai Tak Chu

Optical multi-stability in a nonlinear high-order microring resonator filter

Cite as: APL Photon. 5, 056106 (2020); doi: 10.1063/5.0002941
Submitted: 29 January 2020 • Accepted: 5 May 2020 •
Published Online: 22 May 2020

Li Jin,[1] Luigi Di Lauro,[2,3] Alessia Pasquazi,[2] Marco Peccianti,[2] David J. Moss,[4] Roberto Morandotti,[3,5] Brent E. Little,[6] and Sai Tak Chu[1,a)]

AFFILIATIONS

[1]Department of Physics, City University of Hong Kong, Tat Chee Avenue, Hong Kong, China
[2]Emergent Photonics (EPic) Laboratory, Department of Physics and Astronomy, University of Sussex, Farmer, Brighton, United Kingdom
[3]Institut National de la Recherche Scientifique (INRS), Centre Énergie, Matériaux et Télécommunications (EMT), Varennes, Quebec J3X 1S2, Canada
[4]Centre for Micro-Photonics, Swinburne University of Technology, Hawthorn, VIC 3122, Australia
[5]Institute of Fundamental and Frontier Sciences, University of Electronic Science and Technology of China, Chengdu 610054, China
[6]State Key Lab of Transient Optics and Photonics, Xi'an Institute of Optics and Precision Mechanics, CAS, Xi'an, China

[a)]**Author to whom correspondence should be addressed:** saitchu@cityu.edu.hk

ABSTRACT

We theoretically analyze and experimentally demonstrate optical bi-stability and multi-stability in an integrated nonlinear high-order microring resonator filter based on high-index contrast doped silica glass. We use a nonlinear model accounting for both the Kerr and thermal effects to analyze the instability behavior of the coupled-resonator based filter. The model also accurately predicts the multi-stable behavior of the filter when the input frequency is slightly detuned. To understand the role of the intracavity power distribution, we investigate the detuning of the individual rings of the filter from the optical response with a pump–probe experiment. Such a measurement is performed scanning the filter with a low-power probe beam tuned a few free spectral ranges away from the resonance where the pump is coupled. A comprehensive understanding of the relationship between the nonlinear behavior and the intracavity power distribution for the high-order microring resonator filter will help the design and implementation of future all-optical switching systems using this type of filter.

I. INTRODUCTION

Optical bistability, addressed initially by the pioneering work of Szöke *et al.* in 1969,[1] is a phenomenon that is still of significant interest due to its many applications in ultrafast communications and signal processing.[2–9] Photonic crystals and micro-cavities are two popular geometries for the implementation of all-optical devices such as switches,[10] logic gates,[11] and memories.[12] These devices utilize the free carrier or Kerr induced nonlinear resonance shift to generate their bi-stable behavior.[13] In general, low switching threshold power, high on/off contrast, and multiple operation states are desired in these devices.

Recently, integrated optical ring micro-cavities fabricated with CMOS compatible platforms such as silicon,[14] silicon nitride,[15,16] and high-index-contrast doped silica glass[17–19] have demonstrated excellent nonlinear optical performance. Bistability in these micro-cavities has been investigated both theoretically[20–22] and experimentally,[23–26] based on the Kerr and/or thermo-optical effects, which yield intensity dependent nonlinear responses. In particular, bistability can be triggered at very low power levels in these devices, due to the strong mode confinement, long interaction lengths, and high enhancement of the resonant field.[27,28]

In this framework, high-order resonator filters consisting of multiple cavities have been explored for optical functions such

as slow light[29] and optical buffers.[30] Unlike the linear Lorentzian response of a single ring resonator, in high-order filters, both the bandwidth and shape of the linear high-order filter response can be adjusted by controlling the coupling between the cavities, as well as their relative resonances, thus providing additional degrees of freedom[31,32] in designing these devices. For example, Vlasov *et al.* demonstrated optical switching in a high-order ring resonator filter by thermal tuning of the coupling between the cavities achieved with an external laser.[33] The Kerr nonlinearity has been studied in these systems showing slow-light enhanced four-wave mixing,[34,35] self-pulsation,[36,37] and multistability.[38,39]

Although theoretical models that consider both the optical nonlinear Kerr and thermal effects have previously been proposed and investigated,[24,37] the bistable and, especially, the multi-stable behavior in high-order microresonator filters have not been experimentally demonstrated. In this work, we present both theoretical and experimental studies of the multi-stable response of a fifth-order microring resonator filter. The characterization of the intracavity power distribution in each of the coupled resonators, performed by observing the spectra over different nonlinear regimes, provides a further understanding of the nonlinear dynamics in coupled nonlinear systems. Here, we use a theoretical model based on coupled mode theory[31] to describe a nonlinear high-order microring resonator filter and experimentally verify its multi-stable behavior. We determine the magnitude of the thermally induced resonant frequency shift by comparing experiments with simulations. Finally, we investigate the effects of input frequency detuning on the nonlinear response and derive a method to measure the intracavity power distribution at various stages of the nonlinear operation.

II. THEORETICAL MODEL

Figure 1 shows a schematic of a device consisting of a series of N coupled resonators with the first and last cavities coupled to the input and output waveguides, respectively. The individual resonators are characterized by the energy wave amplitudes for the rings and are represented by the energy amplitude array $\mathbf{a} = [a_1, a_2, \ldots, a_{N-1}, a_N]^T$, where $|a_q|^2$ is the energy in the q^{th} ring defined in units of joules (J). We assume that the power P_{in}, defined in units of watts (W), is excited at the input waveguide, with the input array $\mathbf{s} = \left[-j\mu_i P_{in}^{1/2}, 0, \ldots, 0, 0\right]^T$. Here, μ_i is the input coupling coefficient, in dimensionless units. The time evolution of the energy amplitude $\mathbf{a}(t)$ has the following form:[31,37]

$$\frac{d\mathbf{a}}{dt} = \mathbf{M}\mathbf{a} + \mathbf{s}, \tag{1}$$

where $\mathbf{M}$ is the coupling matrix.

To account for the thermal contribution, an array $\mathbf{\Delta\omega^{(T)}}$ is introduced with $\mathbf{\Delta\omega^{(T)}} = \left[\Delta\omega_1^{(T)}, \Delta\omega_2^{(T)}, \ldots, \Delta\omega_{N-1}^{(T)}, \Delta\omega_N^{(T)}\right]^T$, where $\Delta\omega_q^{(T)}(t)$ is the time-dependent temperature induced resonance shift of the q^{th} ring in unit of rad/s. The amount of thermally induced frequency shift for the individual ring is a function of the instantaneous energy stored in the ring so that the time evolution of $\mathbf{\Delta\omega^{(T)}}$ is expressed as follows:

$$\tau_T \frac{d\mathbf{\Delta\omega^{(T)}}}{dt} = -\mathbf{\Delta\omega^{(T)}} + \gamma_T \mathbf{Q}. \tag{2}$$

Here, τ_T is the thermal relaxation time and γ_T is the thermal coefficient defined in J^{-1} s^{-1} and characterizing the thermally induced frequency shift, while the array $\mathbf{Q} = \left[|a_1|^2, |a_2|^2, \ldots, |a_{N-1}|^2, |a_N|^2\right]^T$ takes into account the energies in each ring. When only the first terms of the right-hand side of Eq. (2) are considered, the equation exhibits an exponential decay type solution, showing that the angular frequency deviation approaches zero with time. In other words, the system gradually becomes stable, and there is no angular frequency deviation with increasing time if no external effect is introduced. The second term in the right-hand side of Eq. (2) describes the angular frequency deviation due to the power dependent thermal effect. It is noted that both the nonlinear Kerr effect and the thermal effect lead to a red shift of the angular frequencies in our simulations and experiments. The cancellation between the nonlinear Kerr effect and the thermal effect is not considered in this model. Other effects including the plasma effect are also not considered.[40–42]

Besides the usual linear $\mathbf{M_L}$ and nonlinear $\mathbf{M_{NL}}$ elements, the coupling matrix $\mathbf{M}$ in the model also consists of an additional thermal coupling matrix element $\mathbf{M_T}$ to account for the thermally induced frequency detuning, such that $\mathbf{M} = \mathbf{M_L} + \mathbf{M_{NL}} + \mathbf{M_T}$, where

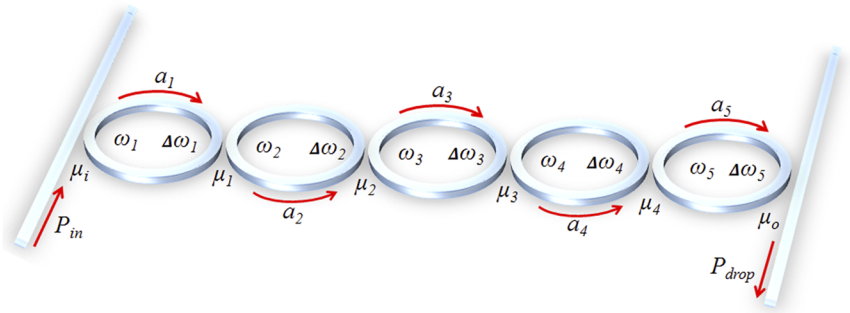

FIG. 1. Schematic of the N^{th} order microring resonator filter with N cascaded rings coupled to two straight waveguides. a_q (q = 1, . . ., N) represents the energy amplitude in the q^{th} ring. P_{in} and P_{drop} represent the power at the input and drop ports, respectively. μ_z ($z = i, o$) represents the normalized coupling coefficients between the straight waveguide and the ring waveguide, and μ_z (z = 1, . . ., N − 1) represents those between the adjacent ring waveguides. $\Delta\omega_q = 2\pi\Delta f_q$ is the angular frequency detuning from the resonance angular frequency ω_q of the q^{th} ring.

$$\mathbf{M_L} = -\begin{bmatrix} j\Delta\omega_1 + \frac{\mu_i^2}{2} + \frac{\mu_L^2}{2} & j\mu_1 & 0 & & \\ j\mu_1 & j\Delta\omega_2 + \frac{\mu_L^2}{2} & j\mu_2 & & \\ & & & & \\ & & & j\mu_{N-2} & j\Delta\omega_{N-1} + \frac{\mu_L^2}{2} & j\mu_{N-1} \\ & \mathrm{O} & & 0 & j\mu_{N-1} & j\Delta\omega_N + \frac{\mu_o^2}{2} + \frac{\mu_L^2}{2} \end{bmatrix}, \tag{3}$$

$$\mathbf{M_{NL}} = -j\gamma_K \begin{bmatrix} |a_1|^2 & & \\ & \ddots & \\ & & |a_N|^2 \end{bmatrix}, \tag{4}$$

$$\mathbf{M_T} = -j \begin{bmatrix} \Delta\omega_1^{(T)} & & \\ & \ddots & \\ & & \Delta\omega_N^{(T)} \end{bmatrix}. \tag{5}$$

Here, $\Delta\omega_q = 2\pi\Delta f_q$ is the angular frequency detuning from the resonance angular frequency ω_q of the q^{th} ring. The coupling coefficients are expressed in dimensionless units, where ${\mu_L}^2/2$ is the decay rate due to intrinsic loss, while ${\mu_i}^2/2$ and ${\mu_o}^2/2$ represent coupling to the input and output waveguides, respectively. The relationships between the power coupling coefficient k_z and the normalized coefficient μ_z are $k_i = \mu_i\sqrt{T_r}$, $k_o = \mu_o\sqrt{T_r}$, $k_1 = \sqrt{\mu_1 T_r}$, $k_2 = \sqrt{\mu_2 T_r}$, $k_3 = \sqrt{\mu_3 T_r}$, and $k_4 = \sqrt{\mu_4 T_r}$, where $T_r = 2\pi R/v_g$ is the roundtrip time, R is the ring radius, and v_g the group velocity.[24] Also, $\mu_L = \sqrt{\alpha c/n_0}$, where α represents loss in units of nepers/m. Here, n_0 is the effective index. In Eq. (4), we have expressed the Kerr effect in $\mathrm{J}^{-1}\ \mathrm{s}^{-1}$, $\gamma_K = \gamma c/(n_0 T_r)$, so that it can be directly compared to the thermal coefficient γ_T. The parameter γ is the nonlinear coefficient due to the Kerr effect in $\mathrm{W}^{-1}\ \mathrm{m}^{-1}$, defined as $\gamma = n_2\omega_0/(cA_{eff})$. Here, n_2 is the Kerr coefficient at the frequency ω_0, c is the speed of light in vacuum, and A_{eff} is the effective area of the cross section of the ring waveguide.

Equations (1)–(5) can be used to obtain a linear relationship between the frequency detuning Δf_q and the instantaneous ring power $P_q = |a_q|^2/T_r$ as follows:

$$\Delta f_q = (\gamma_T + \gamma_K)\frac{T_r P_q}{2\pi}. \tag{6}$$

To study the instability property of the system described by Eqs. (1)–(6), we implemented a linear stability analysis. We introduced a perturbation vector $\boldsymbol{\delta a}$ to the energy amplitude stationary state $\mathbf{a}_f$ and a perturbation vector $\boldsymbol{\delta\Delta\omega}^{(\mathbf{T})}$ to the thermal detuning stationary state $\boldsymbol{\Delta\omega}_f^{(\mathbf{T})}$, where $\boldsymbol{\delta a} = [\delta a_1, \delta a_2, \ldots, \delta a_{N-1}, \delta a_N]^T$, $\mathbf{a_f} = [a_{f,1}, a_{f,2}, \ldots, a_{f,N-1}, a_{f,N}]^T$, and $\boldsymbol{\delta\Delta\omega}^{(\mathbf{T})} = [\delta\Delta\omega_1^{(T)}, \delta\Delta\omega_2^{(T)}, \ldots, \delta\Delta\omega_{N-1}^{(T)}, \delta\Delta\omega_N^{(T)}]^T$ and $\boldsymbol{\Delta\omega}_f^{(\mathbf{T})}$ is referenced to the fixed point $\boldsymbol{\Delta\omega}_f^{(\mathbf{T})} = [\Delta\omega_{f,1}^{(T)}, \Delta\omega_{f,2}^{(T)}, \ldots, \Delta\omega_{f,N-1}^{(T)}, \Delta\omega_{f,N}^{(T)}]^T$. By solving the complex eigenvalue problem of the first order perturbation equations, one can determine the different stability regions of the system.[37]

We now consider the multi-stable behavior of the fifth-order microring resonator filter for theoretical verification and experimental demonstration, starting with its theoretical analysis. Our device is the so-called Chebyshev filter, and it has been designed with a configuration presenting the maximum flat passband.[31] Such a configuration is obtained by setting the six coupling coefficients as $\mu_i = \mu_o$, $\mu_1 = \mu_4 = 0.309{\mu_i}^2$, and $\mu_2 = \mu_3 = 0.178{\mu_i}^2$. A value for μ_i of 1.7665×10^5 is used in the simulation, which corresponds to the power coupling coefficients $k_i = 0.235$. μ_L is assumed to be zero. The relaxation time τ_T for the thermal effect is assumed to be 1 ms in the simulations, which is reasonable and beyond the estimated value of about 1 μs for the thermal relaxation time used in Ref. 24. The static properties of the fifth-order microring resonator filter (given an input laser detuning $\Delta f_p = -2.3$ GHz) calculated and shown in Fig. 2. As an example, the left panel of Fig. 2(a) reports the output power P_{drop} of the steady state as a function of the input power P_{in} for $\gamma_T/\gamma_K = 100$. Here, the blue parts of the multi-stable curve mark the unstable state, while the red parts represent the stable state, where the maximum number of unstable states is proportional to the filter order. In the right subgraph, the real and imaginary parts of the dominant eigenvalue corresponding to such a stationary state are also calculated.[40] The multi-stable regions with positive real parts of the eigenvalues and zero imaginary parts are shaded in blue, matching the threshold boundaries of the multi-stable regions depicted in the left subgraph. Figure 2(b) presents a map of the stable and unstable regions of the filter as a function of both the output power $P_{drop} = |a_N|^2/T_r$ and the ratio γ_T/γ_K. The expected decrease in the output power threshold boundaries of the bi-stable and multi-stable regions is observed when increasing the ratio γ_T/γ_K. The theoretically calculated map for a specific high-order microring resonator filter can be used to fit the experimental results and obtain an estimate of the thermal coefficient γ_T, using the measurement of the Kerr coefficient $\gamma \sim 233\ \mathrm{W}^{-1}\ \mathrm{km}^{-1}$.[16] The linear coupling coefficients can be obtained by fitting the output filter shape.

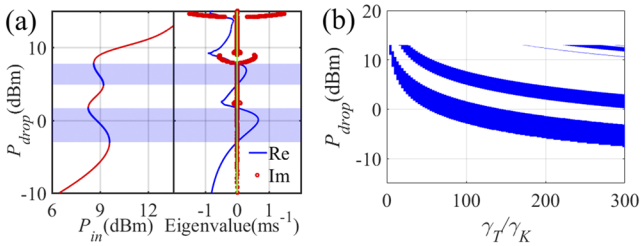

FIG. 2. (a) Left subgraph: simulated multi-stable behavior between P_{drop} and P_{in} in a fifth-order ring resonator filter when considering both Kerr and thermal effects. Right subgraph: real and imaginary parts of the dominant eigenvalues of the perturbation matrix under different P_{drop}. The multi-stable regions are highlighted in light blue, and the unshaded regions are stable. The zero line is marked in green. (b) Multi-stable regions are marked in blue as a map of P_{drop} and the ratio γ_T/γ_K.

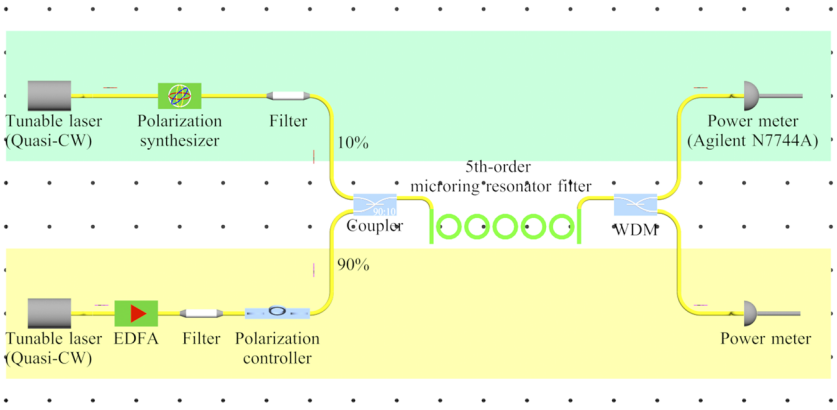

FIG. 3. Schematic of the experimental setup for measuring the linear and nonlinear responses of the fifth-order microring resonator device. The upper combination of a tunable laser and a power meter was used for the linear insertion loss measurement, while the identical lower combination was used for the bi-stable and multi-stable responses measurement. Furthermore, both were used together for the spectral shape evolution measurement.

III. RESULTS AND DISCUSSION

A. Experimental setup and the fifth-order microring resonator filter

Figure 3 shows a schematic of the bi-stability and multi-stability experiments, which also allow for the measurement of the high-order ring resonator filter response. The fifth-order ring resonator filter device consists of a cascade of five microring resonators comprised of high-index (n = 1.7) doped silica glass core waveguides embedded in the silica cladding layer. The five rings have the same radius of 50 μm, where the dimension of the waveguide cross section is 1.45 × 1.45 μm^2. The high-index-contrast waveguide has negligible linear (<0.06 dB/cm) and nonlinear losses with nonlinear parameter γ as high as ~233 W^{-1} km^{-1}.[16] The packaged device was under temperature control with a resolution of 0.01 °C, which corresponded to a shift of 0.2 pm in wavelength. In the bi-stability and multi-stability experiment, the input signal was supplied by a quasi-CW tunable laser with frequency ω_{input} subsequently amplified by an erbium doped fiber amplifier (EDFA). Here, the amplified spontaneous emission noise was suppressed via a 1 nm tunable filter with an extinction ratio greater than 55 dB. A polarization controller was used to adjust the polarization of the input signal into the device. To determine the intracavity power distribution, the evolution of the filter response during the operation was measured with an Agilent insertion/polarization dependent loss (IL/PDL) fast scanning system. Such a system consisted of a quasi-CW laser acting as the probe beam and a polarization synthesizer. To minimize the effect of the scanning signal on the instability behavior, the input frequency ω_{input} and the probe frequency ω_{probe} were kept to within a few free spectral ranges (FSRs) apart, with the power of the probe beam kept at least 30 dB below the input beam. The output signal from the drop port was frequency separated into two paths, with the input and probe signals detected by using two separate detectors.

In the experiment, the linear response of the fifth-order device was measured with the input signal switched off and with the output at the drop port directly connected to the Agilent N7744A optical power detector. Figure 4(a) shows the measured drop response of the device across a span of two FSRs, with FSR = 577 GHz at 1565 nm. The full width at half maximum (FWHM) of the filter pass band is 3.5 GHz. Since the individual rings in the fabricated device are not identical due to fabrication process variations, there is a slight difference in the spectral shape at different resonances, as shown in the enlarged insets. The measured through port loss is 2.75 dB, indicating that the coupling loss between the fiber and the waveguide is <1.5 dB per facet, while the pass band loss is about 4 dB. The pass band near 1560 nm is fitted against the linear model in Ref. 31 to determine the relative detuning between the individual rings of the filter and the corresponding coupling coefficients. The extracted individual detuning is zero, and the coupling coefficients between the ring and waveguide are $\mu_i = 0.13$ and $\mu_o = 0.10$, while between the individual rings are $\mu_1 = 0.015$, $\mu_2 = 0.01$, $\mu_3 = 0.0115$, and $\mu_4 = 0.012$. The loss is 0.22 dB/cm, which corresponds to a coefficient μ_L of about 94.5. The simulated linear response with the above-mentioned parameters is shown in Fig. 4(b).

B. Bi-stable and multi-stable responses

Figure 5(a) shows the simulated nonlinear response at a pump detuning of $\Delta f_p = -3.0$ GHz. Using the extracted filter parameters and according to the steady state analysis in Fig. 2(b), γ_T/γ_K is set to 180 in the simulations to obtain the best agreement with experiments, which tends to apply to all frequencies. In other words, thermal effects form the bulk of the contribution to the observed bi-stable behavior. Based on this thermal coefficient value, we investigated the influence of the input detuning Δf_p on the instability response both experimentally and with the nonlinear model. Figures 5(b) and 5(c) show the simulated and measured responses

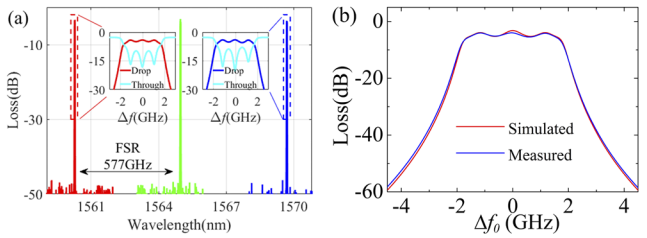

FIG. 4. (a) Linear insertion loss of the resonance of the fifth-order device with an FWHM of 3.5 GHz and FSR of 577 GHz. (b) Simulated linear filter shape at around 1560 nm.

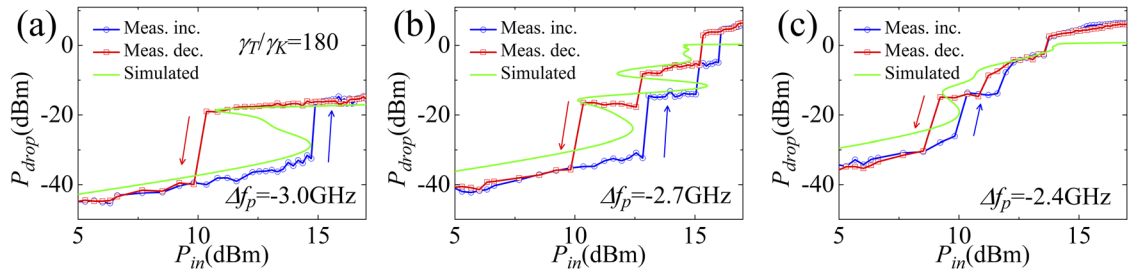

FIG. 5. Plots of the output power P_{drop} at the drop port as a function of the input power P_{in}, for input detunings Δf_p of (a) −3.0 GHz, (b) −2.7 GHz, and (c) −2.4 GHz, respectively. A green and a blue line with circle symbols are used for simulated and measured data taken at increasing powers, while a red line with square symbols and a blue line with circle symbols are used for simulated and measured data taken at decreasing powers. A value γ_T/γ_K = 180 was used in the simulations.

when the input frequency was tuned to Δf_p = −2.7 GHz and −2.4 GHz, respectively. It can be seen from the experimental results that a slight detuning of 0.3 GHz, from −3.0 GHz to −2.7 GHz, induced a drastic change to the response, shifting the behavior from bi-stable to multi-stable, in good agreement with the model. At Δf_p = −2.7 GHz, both the experimental and simulated results show that the variation of the multi-stable response at larger powers creates an additional hysteresis loop.

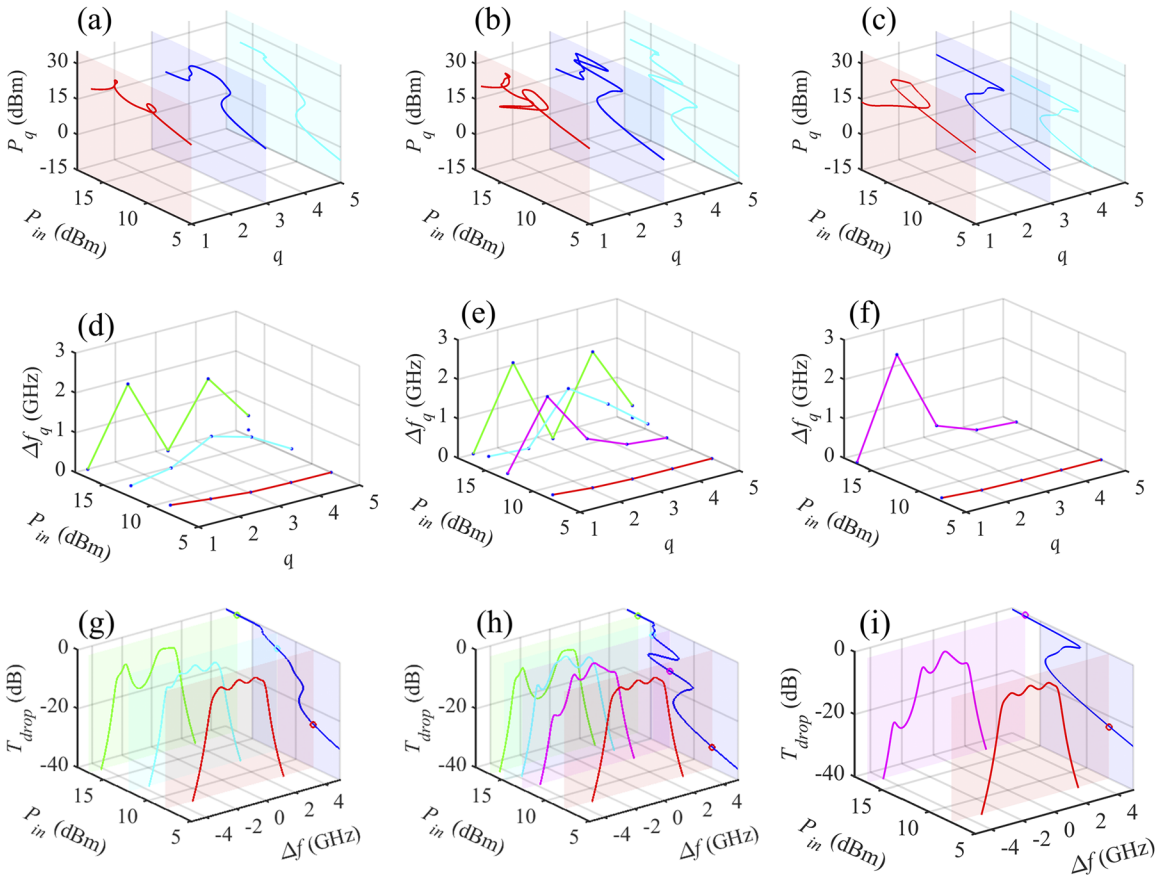

FIG. 6. [(a)–(c)] Simulated responses of individual ring power P_q vs the input power P_{in}, [(d)–(f)] simulated distribution of the individual ring power, and [(g)–(i)] simulated spectral shape, at input detunings Δf_p of −2.4 GHz, −2.7 GHz, and −3.0 GHz, respectively. The three main types of individual ring detuning distribution are colored in red, magenta, and green and presented at different stages. The cyan ones represent the transition state in the unstable region. The normalized simulated bi-stable and multi-stable curves are also plotted in blue in [(g)–(i)], showing the consistence between the bi-stable and multi-stable responses and the spectral shape evolution.

When the detuning is further reduced by an amount of 0.3 GHz at $\Delta f_p = -2.4$ GHz, the additional hysteresis loop observed at $\Delta f_p = -2.7$ GHz becomes narrower with the main bi-stable behavior having a much smaller hysteresis loop compared to that at $\Delta f_p = -3.0$ GHz. The large change in the observed nonlinear behavior with only a slight change of input frequency offers an interesting route for creating tailored pulse shapes by controlling the power, frequency, and spectral width of the input pulse.

C. Intracavity power distribution

To obtain a better understanding of the characteristics of the observed bi-stability and multi-stability behaviors at different stages, we plot in Fig. 6 the simulated intracavity power distribution of the filter stemming from the nonlinear behavior of the individual rings. Figures 6(a)–6(c) show the simulated individual ring powers as a function of increasing P_{in} for different input detuning values. The first three rings near the input waveguide have very different behavior compared to the remaining two rings. The last two rings exhibit classical instability behavior, while the response of the first three rings is more erratic. The detuning variation Δf_q, of the individual rings with P_{in} at different stages of the bi-stable and multi-stable curves, given by Eq. (6), is shown in Figs. 6(d)–6(f).

In the initial stable region where P_{in} is below the lower transition threshold of the bi-stability or multi-stability, the values of Δf_q are small and they all shifted together, nearly "in unison" with each other. Here, the filter pass band slightly shifts in the negative frequency direction with an increase in P_{in} while maintaining its original shape, as marked in red in Figs. 6(g)–6(i). When P_{in} is further increased, the middle rings 2 and 4 encounter larger nonlinear shifts than the other rings because the optical power is larger in these rings. Therefore, the bi-stable and multi-stable curves are determined by the distribution of the individual ring detuning. Figures 6(g)–6(i) show that once the detuning of the individual rings changes, the original near flat-top filter shape becomes distorted and the ripples of the responses become more complex, as marked in magenta and green. This corresponds to the redistribution of the power between the individual rings. Generally, as the shape of the filter response evolves with P_{in}, the spectral power tracks the changes in the bistable and multi-stable responses, as deduced when comparing the bistable and multi-stability curves in blue with the evolution of the spectral shapes in Figs. 6(g)–6(i). Furthermore, it can be seen from Fig. 6 that the frequency of the input power can be used to select the bistable or multi-stable behavior with different intracavity power distributions at different stages. From this analysis, it is clear that the main difference between the instability behaviors in the single-order and high-order ring resonator filters lies in the high-order filter's ability to redistribute its intracavity power, so as to drastically alter the filter response and create much more complex instability dynamics.

Using the scanning probe beam and the Agilent N7744A detector in Fig. 2, the output filter response two FSRs away from the input at various P_{in} was measured to experimentally investigate the evolution of the filter responses. The individual ring detunings Δf_q were extracted by assuming that the coupling coefficients μ_z were fixed at their initial values. The extracted Δf_q as a function of input power P_{in} at three input frequencies are presented in Figs. 7(d)–7(f), showing the distinct distribution of the individual ring detuning in the simulations discussed above. However, it is the evolution of the filter response in Figs. 7(a)–7(c) that clearly demonstrates the basis of the bi-stable and multi-stable behaviors in the experiment.

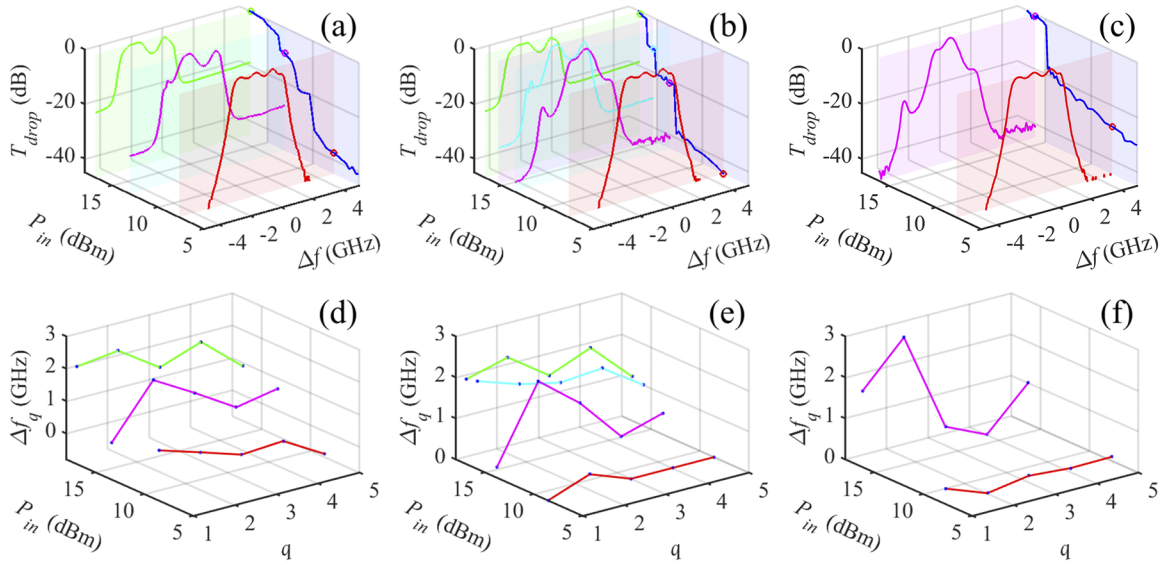

FIG. 7. [(a)–(c)] Normalized measured spectral shape evolution T_{drop} and [(d)–(f)] extracted individual ring detuning Δf_q, as a function of the input power P_{in} at input detunings Δf_p of −2.4 GHz, −2.7 GHz, and −3.0 GHz, respectively. The normalized measured bi-stable and multi-stable curves are also plotted in blue in [(a)–(c)].

IV. CONCLUSION

We theoretically analyze and experimentally demonstrate optical bi-stability and multi-stability in a high-order integrated nonlinear microring resonator filter. We present a nonlinear model for the analysis of instability in the N^{th} order resonator filter, which includes both thermal and Kerr effects. The model is used to provide insight into the measured bistable and multi-stable behavior in a fifth-order microring resonator filter. By comparing the simulated and measured bi-stable responses, the thermal effect has been found to dominate the response, being two orders of magnitude larger than the Kerr effect. Using an additional scanning probe beam and a separate detector, we measured the evolution of the filter response for different input powers. We observed that the detunings of the individual rings all shifted uniformly at low-power, while they had different distributions at different stages of the bi-stable and multi-stable curves at high-power. We have shown that the different nonlinear filter responses in the high-order ring resonator filter are due to the redistribution of the optical power within the single resonators. The complex instability behavior achieved in the high-order ring resonator filter can be potentially exploited to produce advanced switching devices.

ACKNOWLEDGMENTS

The authors acknowledge the support of the EPSRC, Industrial Innovation Fellowship Programme, under Grant No. EP/S001018/1, from INNOVATE UK, project "IOTA" Grant Agreement No. EP/R043566/1 and from the University of Sussex RDF program. This project has received funding from the European Research Council (ERC) under the European Union's Horizon 2020 research and innovation program, Grant Agreement No. 725046. A.P. acknowledges the support of the EPSRC, Industrial Innovation Fellowship Programme, under Grant No. EP/S001018/1, from INNOVATE UK, project "IOTA" Grant Agreement No. EP/R043566/1 and from the University of Sussex RDF program. MP has received funding from the European Research Council (ERC) under the European Union's Horizon 2020 research and innovation program, Grant Agreement No. 725046. S.T.C. acknowledges support from the Research Grant Council of Hong Kong (GRF No. 9042663). B.E.L. acknowledges support from the Strategic Priority Research Program of the Chinese Academy of Sciences (Grant No. XDB24030300). R.M. is affiliated to 5 as an adjoint faculty and acknowledges funding by the Natural Sciences and Engineering Research Council of Canada (NSERC) through the Strategic, Discovery, and Acceleration Grants Schemes, by the MESI PSR-SIIRI Initiative in Quebec and by the Canada Research Chair Program.

DATA AVAILABILITY

The data that support the findings of this study are available from the corresponding author upon reasonable request.

REFERENCES

[1] A. Szöke, V. Daneu, J. Goldhar, and N. A. Kurnit, "Bistable optical element and its applications," Appl. Phys. Lett. **15**, 376 (1969).
[2] S. D. Smith, "Optical bistability: Towards the optical computer," Nature **307**, 315 (1984).
[3] M. F. Yanik, S. Fan, M. Soljačić, and J. D. Joannopoulos, "All-optical transistor action with bistable switching in a photonic crystal cross-waveguide geometry," Opt. Lett. **28**, 2506 (2003).
[4] O. Wada, "Femtosecond all-optical devices for ultrafast communication and signal processing," New J. Phys. **6**, 183 (2004).
[5] V. R. Almeida, C. A. Barrios, R. R. Panepucci, and M. Lipson, "All-optical control of light on a silicon chip," Nature **431**, 1081 (2004).
[6] M. Notomi, A. Shinya, S. Mitsugi, G. Kira, E. Kuramochi, and T. Tanabe, "Optical bistable switching action of Si high-Q photonic-crystal nanocavities," Opt. Express **13**, 2678 (2005).
[7] M. W. Feise, I. V. Shadrivov, and Y. S. Kivshar, "Bistable diode action in left-handed periodic structures," Phys. Rev. A **71**, 037602 (2005).
[8] S. Li and X. Cai, "High-contrast all optical bistable switching in coupled nonlinear photonic crystal microcavities," Appl. Phys. Lett. **96**, 131114 (2010).
[9] C. Y. Qiu, Y. X. Yang, C. Li, Y. F. Wang, K. Wu, and J. P. Chen, "All-optical control of light on a graphene-on-silicon nitride chip using thermo-optic effect," Sci. Rep. **7**, 17046 (2017).
[10] K. Nozaki, T. Tanabe, A. Shinya, S. Matsuo, T. Sato, H. Taniyama, and M. Notomi, "Sub-femtojoule all-optical switching using a photonic-crystal nanocavity," Nat. Photonics **4**, 477 (2010).
[11] Q. Xu and M. Lipson, "All-optical logic based on silicon micro-ring resonators," Opt. Lett. **15**, 924 (2007).
[12] K. Nozaki, A. Shinya, S. Matsuo, Y. Suzaki, T. Segawa, T. Sato, Y. Kawaguchi, R. Takahashi, and M. Notomi, "Ultralow-power all-optical RAM based on nanocavities," Nat. Photonics **6**, 248 (2012).
[13] R. W. Eason and A. Millar, *Nonlinear Optics in Signal Processing* (Springer Science+Business Media, Chapman and Hall, 1993).
[14] J. Leuthold, C. Koos, and W. Freude, "Nonlinear silicon photonics," Nat. Photonics **4**, 535 (2010).
[15] J. S. Levy, A. Gondarenko, M. A. Foster, A. C. Turner-Foster, A. L. Gaeta, and M. Lipson, "CMOS-compatible multiple-wavelength oscillator for on-chip optical interconnects," Nat. Photonics **4**, 37 (2010).
[16] D. J. Moss, R. Morandotti, A. L. Gaeta, and M. Lipson, "New CMOS-compatible platforms based on silicon nitride and Hydex for nonlinear optics," Nat. Photonics **7**, 597 (2013).
[17] M. Ferrera, L. Razzari, D. Duchesne, R. Morandotti, Z. Yang, M. Liscidini, J. E. Sipe, S. Chu, B. E. Little, and D. J. Moss, "Low-power continuous-wave nonlinear optics in doped silica glass integrated waveguide structures," Nat. Photonics **2**, 737 (2008).
[18] L. Razzari, D. Duchesne, M. Ferrera, R. Morandotti, S. Chu, B. E. Little, and D. J. Moss, "CMOS-compatible integrated optical hyper-parametric oscillator," Nat. Photonics **4**, 41 (2010).
[19] M. Peccianti, A. Pasquazi, Y. Park, B. E. Little, S. T. Chu, D. J. Moss, and R. Morandotti, "Demonstration of a stable ultrafast laser based on a nonlinear microcavity," Nat. Commun. **3**, 765 (2012).
[20] I. D. Rukhlenko, M. Premaratne, and G. P. Agrawal, "Analytical study of optical bistability in silicon ring resonators," Opt. Lett. **35**, 55 (2010).
[21] Y. Dumeige and P. Feron, "Stability and time-domain analysis of the dispersive tristability in microresonators under modal coupling," Phys. Rev. A **84**, 043847 (2011).
[22] L. D. Lauro, J. Li, D. J. Moss, R. Morandotti, S. T. Chu, M. Peccianti, and A. Pasquazi, "Parametric control of thermal self-pulsation in micro-cavities," Opt. Lett. **42**, 3407 (2017).
[23] T. Carmon, L. Yang, and K. J. Vahala, "Dynamical thermal behavior and thermal self-stability of microcavities," Opt. Express **12**, 4742 (2004).
[24] A. E. Fomin, M. L. Gorodetsky, I. S. Grudinin, and V. S. Ilchenko, "Nonstationary nonlinear effects in optical microspheres," J. Opt. Soc. Am. B **22**, 459 (2005).
[25] G. Priem, P. Dumon, W. Bogaerts, D. Van Thourhout, G. Morthier, and R. Baets, "Optical bistability and pulsating behavior in silicon-on-insulator ring resonator structures," Opt. Express **13**, 9623 (2005).
[26] S. Chen, L. Zhang, Y. Fei, and T. Cao, "Bistability and self-pulsation phenomena in silicon microring resonators based on nonlinear optical effects," Opt. Express **20**, 7454 (2012).

[27]D. K. Armani, T. J. Kippenberg, S. M. Spillane, and K. J. Vahala, "Ultra-high-Q toroid microcavity on a chip," Nature **421**, 925 (2003).
[28]F. Ramiro-Manzano, N. Prtljaga, L. Pavesi, G. Pucker, and M. Ghulinyan, "Thermo-optical bistability with Si nanocrystals in a whispering gallery mode resonator," Opt. Lett. **38**, 3562 (2013).
[29]F. Xia, L. Sekaric, and Y. Vlasov, "Ultracompact optical buffers on a silicon chip," Nat. Photonics **1**, 65 (2007).
[30]M. Notomi, E. Kuramochi, and T. Tanabe, "Large-scale arrays of ultrahigh-Q coupled nanocavities," Nat. Photonics **2**, 741 (2008).
[31]B. E. Little, S. T. Chu, H. A. Haus, J. Foresi, and J.-P. Laine, "Microring resonator channel dropping filters," J. Lightwave Technol. **15**, 998 (1997).
[32]A. Yariv, Y. Xu, R. K. Lee, and A. Scherer, "Coupled-resonator optical waveguide: A proposal and analysis," Opt. Lett. **24**, 711 (1999).
[33]Y. Vlasov, W. M. J. Green, and F. Xia, "High-throughput silicon nanophotonic wavelength-insensitive switch for on-chip optical networks," Nat. Photonics **2**, 242 (2008).
[34]A. Melloni, F. Morichetti, and M. Martinelli, "Four-wave mixing and wavelength conversion in coupled-resonator optical waveguides," J. Opt. Soc. Am. B **25**, C87 (2008).
[35]F. Morichetti, A. Canciamilla, C. Ferrari, A. Samarelli, M. Sorel, and A. Melloni, "Travelling-wave resonant four-wave mixing breaks the limits of cavity-enhanced all-optical wavelength conversion," Nat. Commun. **2**, 296 (2011).
[36]V. Grigoriev and F. Biancalana, "Resonant self-pulsations in coupled nonlinear microcavities," Phys. Rev. A **83**, 043816 (2011).
[37]S. Abdollahi and V. Van, "Analysis of optical instability in coupled microring resonators," J. Opt. Soc. Am. B **31**, 3081 (2014).
[38]Y. Dumeige and P. Féron, "Dispersive tristability in microring resonators," Phys. Rev. E **72**, 066609 (2005).
[39]Y. Dumeige, L. Ghisa, and P. Féron, "Dispersive multistability in microring resonators," J. Opt. A: Pure Appl. Opt. **8**, S483 (2006).
[40]A. Armaroli, S. Malaguti, G. Bellanca, S. Trillo, A. de Rossi, and S. Combrié, "Oscillatory dynamics in nanocavities with noninstantaneous Kerr response," Phys. Rev. A **84**, 053816 (2011).
[41]A. de Rossi, M. Lauritano, S. Combrié, Q. Vy Tran, and C. Husko, "Interplay of plasma-induced and fast thermal nonlinearities in a GaAs-based photonic crystal nanocavity," Phys. Rev. A **79**, 043818 (2009).
[42]T. Uesugi, B.-S. Song, T. Asano, and S. Noda, "Investigation of optical nonlinearities in an ultra-high-Q Si nanocavity in a two-dimensional photonic crystal slab," Opt. Express **14**, 377 (2006).